J. Fluid Mech. (1995), *vol.* 286, *pp.* 379–404

A numerical study of the shearing motion of emulsions and foams

By XIAOFAN LI, HUA ZHOU AND C. POZRIKIDIS

Department of Applied Mechanics and Engineering Sciences,
University of California at San Diego, La Jolla, CA 92093-0411, USA

(Received 2 June 1994 and in revised form 14 October 1994)

A numerical study is presented of the motion of two-dimensional, doubly periodic, dilute and concentrated emulsions of liquid drops with constant surface tension, subject to a simple shear flow. The numerical method is based on a boundary integral formulation that employs a Green's function for doubly periodic Stokes flow, computed using the Ewald summation method. Under the assumption that the viscosity of the drops is equal to that of the ambient fluid, the motion is examined in a broad range of capillary numbers, volume fractions, and initial geometrical configurations. The latter include square and hexagonal lattices of circular and closely packed hexagonal drops with rounded corners. Based on the nature of the asymptotic motion at large times, a phase diagram is constructed separating regions where periodic motion is established, or the emulsion is destabilized due to continued elongation or coalescence of intercepting drops. Comparisons with previous computations for bounded systems illustrate the significance of the walls on the evolution and rheological properties of an emulsion. It is shown that the shearing flow is able to stabilize a concentrated emulsion against the tendency of the drops to become circular and coalesce, thereby allowing for periodic evolution even when the volume fraction of the suspended phase might be close to that for dry foam. This suggests that the imposed shearing flow plays a role similar to that of the disjoining pressure for stationary foam. At high volume fractions, the geometry of the microstructure and flow at the Plateau borders and within the thin films separating adjacent drops are illustrated and discussed with reference to the predictions of the quasi-steady theory of foam. Although the accuracy of certain fundamental assumptions underlying the quasi-steady theory is not confirmed by the numerical results, we find qualitative agreement regarding the basic geometrical features of the evolving microstructure and effective rheological properties of the emulsion.

1. Introduction

Suspensions of liquid drops and gas bubbles are known to exhibit a broad range of rheological behaviours dependent primarily upon the volume fraction of the suspended phase, but also upon the physical properties of the fluids and fluid interfaces. The behaviour at low volume fractions may be analysed by conducting studies of the individual drop or bubble motions and deformations in virtually infinite definable flows (Kennedy, Pozrikidis & Skalak 1994; Pozrikidis 1994; Stone 1994), but studying the motion at moderate and high volume fractions is challenged by the geometrical complexity of the interfacial configurations and by uncertainties in identifying the particle distributions and dominant modes of fluid motion at close particle contact.

The structure and motion of an emulsion at high volume fractions is best described in terms of the shape and deformation of the thin films that separate neighbouring bubbles or drops, and their multiple junctions called Plateau borders (Kraynik 1988). This point of view led Princen (1979, 1983) and a number of subsequent authors to consider the geometrical structure of the films and Plateau borders in a model system consisting of an ordered two-dimensional network of hexagonal drops placed on the vertices of a regular doubly periodic hexagonal lattice. When the motion is due to an imposed simple shear flow, the displacements of the centres of the drop and mid-points of the thin films are affine with respect to the applied macroscopic strain, and the instantaneous structure of the foam may be determined from the instantaneous strain without reference to the history of deformation (Khan 1985; Pacetti 1985; Kraynik & Hansen 1986). To carry out the analysis, it is necessary to make several assumptions regarding the geometry of the instantaneous structure including, in particular, the magnitude of the angles subtended by the films and the curvature of the interfaces enclosing the Plateau borders. The fluid flow inside the bubbles or drops and within the thin films and Plateau borders is considered to be of secondary importance and does not enter the model to this level of approximation.

Several subsequent attempts have been made to account for the effect of the fluid flow on both the geometry of the foam and its effective constitutive equation. Khan & Armstrong (1987) and Kraynik & Hansen (1987) accounted for the effect of the film-level flows on the geometry of the foam and effective stress tensor. Their results rely on the assumption that the films are instantaneously subjected to uniform extensional flows during the deformation. The validity of this assumption was questioned by Schwartz & Princen (1987) and Reinelt & Kraynik (1989, 1990) who used the film withdrawal mechanism of Mysels, Shinoda & Frankel (1959) to develop an improved hydrodynamic model. Their final expression for the effective stress contains a hydrodynamic correction term that involves the capillary number *Ca* expressing the ratio between shearing viscous forces and surface tension.

Reinelt & Kraynik (1989, 1990), in particular, considered the effect of the fluid flow on the geometry of the foam in the limit of small capillary number. A key assumption in their model is that the distribution of surfactants over the interfaces is adjusted to render the interfaces at the transition region next to the Plateau borders inextensible, and yield a distribution of surface tension that is consistent with the assumed model of fluid flow. Their results showed that the foam exhibits elastic behaviour, the effective viscosity increases with increasing volume fraction of the suspended phase, and the viscous contribution to the instantaneous effective stress scales with the capillary number raised to the $\frac{2}{3}$ power.

In this paper we present a numerical study of the motion of dilute and concentrated emulsions of liquid drops in simple shear flow. The equations governing the fluid flow within each phase are solved exactly without any approximations, except from those involved in the assumptions of low-Reynolds-number flow, and the stipulation that the interfaces exhibit constant surface tension. The latter precludes the presence of surfactants. To the authors' knowledge, this is the first attempt to quantify the hydrodynamics of unbounded densely dispersed fluid systems relaxing the assumptions of the lubrication models.

Adopting Princen's approach, we consider monodisperse, doubly periodic, ordered, two-dimensional systems. The numerical studies are conducted by solving a series of initial-value problems corresponding to different initial drop shapes and lattice configurations, and the results span the whole range from the dilute limit where drop interactions are insignificant, to the highly concentrated limit where drop interactions are dominant. Comparisons between the present results for doubly periodic systems and those of Zhou & Pozrikidis (1993*a*, *b*), for emulsions within a channel with parallel walls, allow us to assess the significance of the boundaries on the structure and effective rheological properties of an emulsion. Furthermore, comparisons between the present results at high volume fractions and the predictions of the theories of foam allow us to assess the accuracy of the approximations involved in previous studies.

An important issue pertinent to the behaviour of a concentrated emulsion at a volume fraction higher than that corresponding to maximum packing of circular drops is its long-term viability in the absence of stabilizing intermolecular forces. As the drops press against each other in an effort to obtain a circular shape, the intervening thin films rupture and the emulsion breaks down in a finite time. The action of intermolecular forces has been implicit in previous models of foam through the presence of black film zones and the assumed stable behaviour of the transient zones connecting the thin films to the Plateau borders, but is not included in the present formulation. We shall show, however, that, within a certain range of parameters, the shear flow is able to stabilize the thin films by means of rolling interfacial motions, thereby allowing for periodic behaviour that turns out to be similar to that prescribed in previous studies.

The present computations are carried out on the basis of the method of interfacial dynamics, which is an advanced implementation of the boundary integral method (Pozrikidis 1992; Zhou & Pozrikidis 1993*a*, *b*). One crucial aspect of the mathematical formulation is the use of a new Green's function representing the doubly periodic flow produced by two-dimensional point forces that are located at the nodes of a generally non-orthogonal two-dimensional lattice. We find that the most efficient way of computing this Green's function is by integrating the corresponding three-dimensional periodic Green's function in one direction, thus maintaining the crucial benefits of the Ewald summation method (Beenaker 1986; Brady *et al.* 1988; Pozrikidis 1993). The efficient computation of the Green's function is indispensable for the practical feasibility of the present numerical study.

2. Problem formulation

We consider the evolution of a two-dimensional, doubly periodic, monodisperse suspension of deformable liquid drops with viscosity $\lambda\mu$ suspended in an ambient fluid with viscosity μ. The surface tension of the interfaces γ is assumed to be constant. At the initial instant, the drops are arranged at the vertices of a regular square or hexagonal lattice as shown in figure 1(*a*, *b*). The initial configuration of the suspension is defined by specifying (i) the two lattice base vectors $\boldsymbol{a}_1$ and $\boldsymbol{a}_2$, which are assumed to be of equal length L, (ii) the drop volume fraction, ϕ, and (iii) the initial drop shape. When the base vectors are perpendicular to each other we obtain a rectangular lattice, whereas when they form an angle of $2\pi/3$ we obtain a hexagonal lattice.

The motion is driven by an external unbounded simple shear flow with shear rate k, $\boldsymbol{u}^{\infty} = (kx_2, 0)$, directed along the base vector $\boldsymbol{a}_1$. The base vectors behave like material lines and are thus convected by the unperturbed shear flow. The base vector $\boldsymbol{a}_1$ remains constant independent of time, $\boldsymbol{a}_1 = (L, 0)$, whereas $\boldsymbol{a}_2 = \boldsymbol{a}_2(t = 0) + (ka_{2,y}t, 0)$, where $a_{2,y}$ is the y-component of $\boldsymbol{a}_2$.

When the Reynolds number Re based on the shear rate k and the equivalent drop radius a is small, $Re = ka^2/\nu$ where ν is the kinematic viscosity, the flow is governed

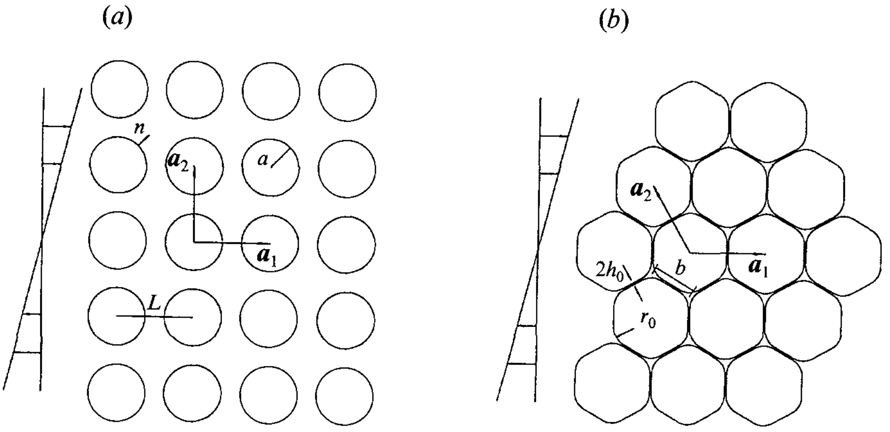

FIGURE 1. Schematic illustration of a doubly periodic suspension of two-dimensional drops in infinite simple shear flow. (*a*) Circular drops with radius a on a square lattice with base vectors $\boldsymbol{a}_1$ and $\boldsymbol{a}_2$. (*b*) Hexagonal drops with rounded corners on a regular hexagonal lattice. Shown are thin films of thickness $2h_0$, the characteristic cell size b, and Plateau borders with radii of curvature r_0.

by the continuity equation

$$\nabla \cdot \boldsymbol{u} = 0 \tag{2.1}$$

and the Stokes equation

$$-\nabla p + \lambda \mu \nabla^2 \boldsymbol{u} = 0 \quad \text{or} \quad -\nabla p + \mu \nabla^2 \boldsymbol{u} = 0 \tag{2.2}$$

inside or outside the drops.

Following the standard boundary integral formulation for Stokes flow, under the additional stipulation that $\lambda = 1$, we obtain the velocity field in terms of the incident flow $\boldsymbol{u}^\infty$ and a single-layer potential due to the discontinuity in surface force across the interfaces $\Delta \boldsymbol{f}$,

$$u_j(\boldsymbol{x}_0) = u_j^\infty(\boldsymbol{x}_0) - \frac{1}{4\pi\mu} \int_C \Delta f_i(\boldsymbol{x}) G_{ij}^{DP}(\boldsymbol{x}, \boldsymbol{x}_0)\, \mathrm{d}l(\boldsymbol{x}) \tag{2.3}$$

(Pozrikidis 1992, Chapter 5). The integration is over the interface of an arbitrary drop C in the lattice. Equation (2.3) is valid both inside and outside the drops as well as at the interfaces. The assumption $\lambda = 1$ allows us to obtain the interfacial velocity simply by computing a line integral instead of solving a Fredholm integral equation of the second kind as required when $\lambda \neq 1$ (Pozrikidis 1992).

An important feature of the boundary integral representation (2.3) is the use of the Green's function $\boldsymbol{G}^{DP}$ representing the doubly periodic flow due to a two-dimensional periodic lattice of point forces with base vectors $\boldsymbol{a}_1$ and $\boldsymbol{a}_2$. The superscript ^{DP} stands for doubly periodic. Details on the derivation and numerical computation of $\boldsymbol{G}^{DP}$ in terms of Ewald sums are given in the Appendix.

Denoting the curvature of the drop interface in the (x_1, x_2)-plane by κ and the unit vector normal to the interface pointing into the ambient fluid by $\boldsymbol{n}$, we express the difference of surface force across the drop interface as $\Delta \boldsymbol{f} = \gamma \kappa \boldsymbol{n}$. Substituting this expression into (2.3), setting $\boldsymbol{u}^\infty = (kx_2, 0)$, and non-dimensionalizing all variables using the equivalent drop radius a as characteristic length, ka as characteristic velocity,

μk as characteristic stress, we obtain the following dimensionless integral equation:

$$u_j(\boldsymbol{x}_0) = \delta_{j1} x_{0,2} - \frac{1}{4\pi Ca} \int_C \kappa(\boldsymbol{x}) n_i(\boldsymbol{x}) G_{ij}^{DP}(\boldsymbol{x}, \boldsymbol{x}_0)\, \mathrm{d}l(\boldsymbol{x}). \tag{2.4}$$

The drop capillary number Ca in (2.4) is defined as $ka\mu/\gamma$. It is clear from equation (2.4) that the flow field is determined from knowledge of the instantaneous position and shape of the drops and the value of Ca.

Since the suspension is homogeneous in both the x_1 and x_2 directions, the effective stress tensor $\boldsymbol{\sigma}^{EFF}$ can be calculated in terms of volume average of the local stress field over a unit cell as discussed by Batchelor (1970). Here we adopt the alternative but equivalent formalism of Zhou & Pozrikidis (1993*b*) and define

$$\sigma_{ij}^{EFF} = 2\mu e_{ij}^{EFF} + \frac{2}{A} \Sigma_{ij}, \tag{2.5}$$

where e^{EFF} represents the average of the rate of strain tensor given by $e_{ij}^{EFF} = \frac{1}{2}k(1 - \delta_{ij})$, A is the total area of a unit cell,

$$\Sigma_{ij} = \frac{1}{2}\gamma \int_C t_i t_j \, \mathrm{d}l \tag{2.6}$$

is the surface-energy tensor, and $\boldsymbol{t}$ is the unit vector tangential to the interface pointing in the counter-clockwise direction. The effective viscosity μ_{EFF} and normal stress difference $\mathcal{N}$ are defined as

$$\mu_{EFF} = \tfrac{1}{2}\sigma_{12}^{EFF} / e_{12}^{EFF}, \quad \mathcal{N} = \sigma_{11}^{EFF} - \sigma_{22}^{EFF}. \tag{2.7}$$

3. Numerical methods

The numerical procedure is similar to that developed and implemented by Zhou & Pozrikidis (1993*a*, *b*) with some minor variations. Briefly, we describe the interface of a drop using a set of marker points, and approximate its shape using cubic splines that are defined with respect to arclength around the drop. At each time step, we adjust the distribution of the marker points by adding new points or removing existing points so as to (i) maintain the distance between two neighbouring marker points within preset maximum and minimum thresholds, and (ii) maintain the magnitude of the angles subtended by the circular arcs that connect three successive points below another threshold value.

The integral in (2.4) is computed using the four-point Gauss–Legendre quadrature over each boundary segment. As $\boldsymbol{x}$ approaches $\boldsymbol{x}_0$, the kernel $G_{ij}^{DP}(\boldsymbol{x}, \boldsymbol{x}_0)$ behaves like $\ln r$, where $r = |\boldsymbol{x} - \boldsymbol{x}_0|$. To remove this logarithmic singularity, we replace $\kappa(\boldsymbol{x})$ by $\kappa(\boldsymbol{x}) - \kappa(\boldsymbol{x}_0)$ in the numerical integration of (2.4). The incompressibility of the flow due to a point force guarantees that this modification does not alter the value of the original integral. An apparent difficulty arises when two drops move close to each other but are still separated by a thin film, which means that $\boldsymbol{x}$ approaches $\boldsymbol{x}_0$ from a neighbouring interface, but we find that the integral in (2.4) is still computed accurately using the Gaussian quadrature due to the weak nature of the singularity of the integrand.

To advance the position of the marker points we use the Runge–Kutta–Fehlberg methods of order three (RKF23) or five (RKF45). The higher-order adaptive time-step method RKF45 becomes necessary for handling the stiffness of the differential equations at high volume fractions where the velocity gradients are large.

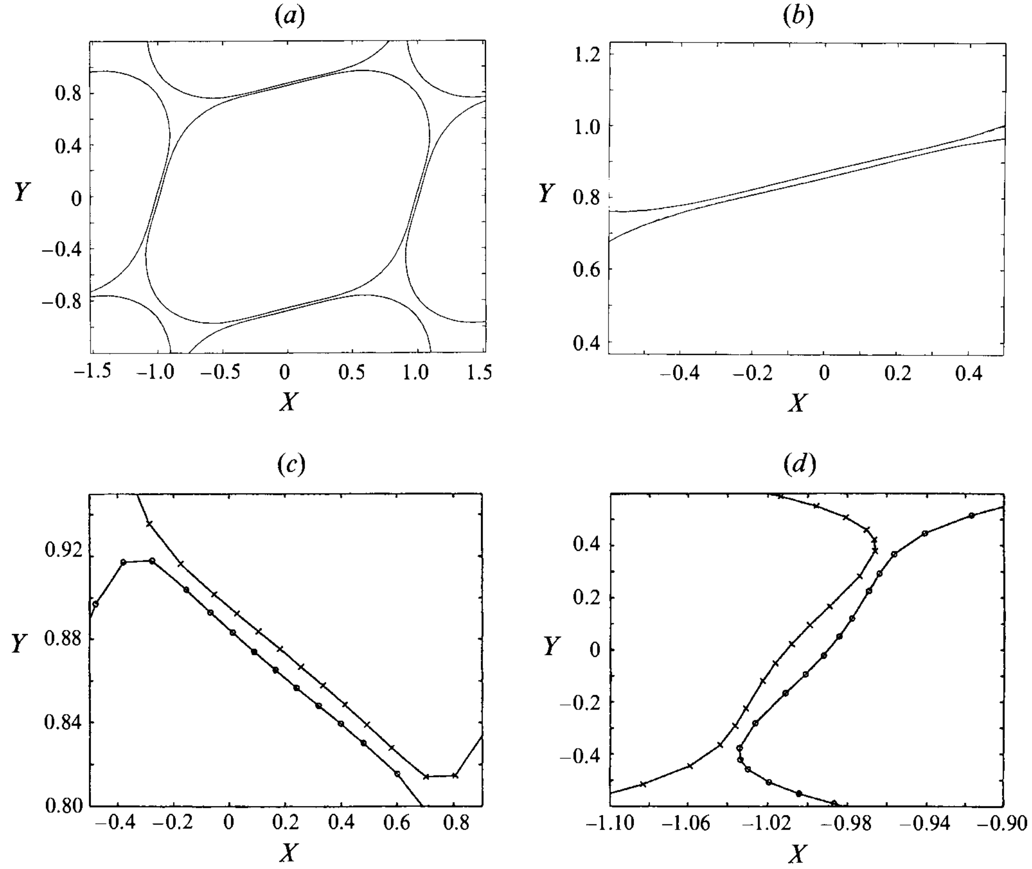

FIGURE 2. (*a*) Comparison of drop shapes at time $kt = 1/\sqrt{3}$ for $\phi = 0.93$ and $Ca = 0.02$: - - - - -, initial number of marker points $N = 60$; ———, a refined computation with $N = 84$ (almost indistinguishable on the figures). (*b*) A close look at the horizontal film region of (*a*). (*c,d*) Magnified plots of the thin films enclosed by the rectangles shown in figure 7(*j*), showing the marker points, o and x, around the drop interface. In all subsequent figures of drop profiles, the horizontal and vertical axes will correspond to the dimensionless distances $X = 2x/L, Y = 2y/L$, where $\boldsymbol{a}_1 = (L, 0)$.

To demonstrate the accuracy and convergence of the numerical method, we compare the results of two computations with identical initial conditions corresponding to volume fraction $\phi = 0.93$ and $Ca = 0.02$, but with different initial number of marker points, $N = 60$ and $N = 84$. In figure 2(*a*, *b*) we plot with solid and dashed lines the profiles of the interfaces at time $kt = 1/\sqrt{3}$, at which point the number of marker points has increased, respectively, to $N = 66$ and $N = 98$ due to the adaptive point redistribution. Small differences can be detected only near the high curvature regions and are of the order of the error of the numerical method used to carry out the spline interpolation.

When the drops are close to each other, a sufficiently fine discretization of the interfaces is necessary in order to obtain accurate solutions. To illustrate the discrete interfacial representation at small drop separations and associated distribution of marker points at high volume fractions beyond maximum packing, we zoom into the thin film regions indicated by the rectangles of figure 7(*j*) (for discussions see §6.1) and present the enlarged pictures in figure 2(*c*, *d*). Since in the blown-up pictures the length scales in the x_1 and x_2 directions are different, figure 2(*c*, *d*) should be inspected in conjunction with figure 7(*j*). To this end, it is important to note that the boundary integral method does not require that the spacing between the marker points be smaller than the minimum distance between two neighbouring interfaces, unless the curvature is prohibitively large. The overall accuracy of the numerical method is determined by the computations of the interfacial curvature and weakly singular integrals. In all cases, the change in the area of a drop due to numerical error was less than 0.2% during the course of a complete computation.

A complete computation typically required 2 hr to 8 hr of CPU time on the CRAY C90 computer of the San Diego Supercomputer Center.

4. Square lattices

We begin by considering monodisperse suspensions with initially circular drops of radius *a*, placed at the vertices of a square lattice with length *L* as shown in figure 1(*a*). The maximum volume fraction corresponding to touching drops with $L/a = 2$ is $\phi^S_{MAX} = \pi/4 \approx 0.7854$.

Not surprisingly, we find that when $L/a = 8$, corresponding to a small volume fraction of $\phi = 0.04909$, the drops deform as if they were suspended alone in an infinite shear flow. At small values of *Ca*, the drops elongate and reach an almost stationary shape while exhibiting small oscillations due to the overpassing and underpassing arrays. The nearly stationary asymptotic shapes become more elongated as the capillary number is increased, and at a critical capillary number, estimated to be between 1.00 and 1.75, they continue to deform and elongate under the action of the shear flow.

To identify the significance of boundary walls on the flow of an emulsion, we compare the present results for doubly periodic systems to those reported in a previous paper for simply periodic suspensions in plane Couette flow between two rigid walls (Zhou & Pozrikidis 1993*a*), and find identical behaviours. Comparing, in particular, the corresponding evolutions of the Taylor deformation parameter defined as $D = (A - B)/(A + B)$, where *A* and *B* are respectively the maximum and minimum dimension of the drop, and the drop orientation angle θ computed using the eigenvectors of the drop inertial tensor, with those shown in figure 2(*a*, *b*) of Zhou & Pozrikidis (1993*a*) for a range of values of *Ca*, we find that they are virtually indistinguishable. This agreement serves to confirm the accuracy of the numerical method.

Interactions between drops in neighbouring layers become noticeable when the drop volume fraction is increased to 0.4418, corresponding to $L/a = 8/3$. The effect of the overpassing drops is manifested by strong oscillation in the drop shape and associated geometrical properties including *D* and θ. As in the case of small volume fractions, we find that there exists a critical capillary number, placed between 0.25 and 0.75, under which the drops deform and execute periodic motion and above which the drops continue to deform without ever reaching a periodic state.

Comparing the present results to those of Zhou & Pozrikidis (1993*a*) for bounded Couette flow shows that the critical capillary number for doubly periodic flow is higher than that for bounded flow. This is because the mutual interactions between the drops are weaker than the interactions between the drops and the solid walls.

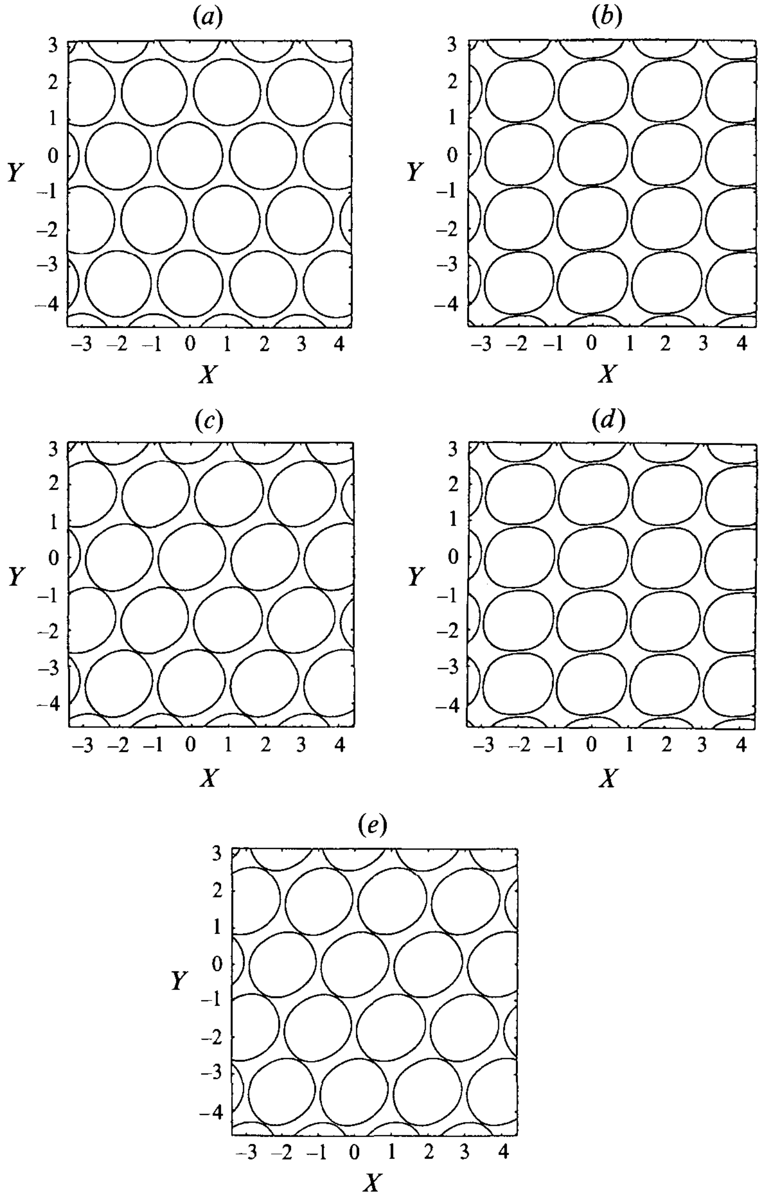

FIGURE 3. Drop profiles evolving from an initially hexagonal lattice of circular drops with $\phi = 0.7495$ and $Ca = 0.02527$ at time (*a*) $kt = 0$, (*b*) $1/\sqrt{3}$, (*c*) $2/\sqrt{3}$, (*d*) $3/\sqrt{3}$, (*e*) $4/\sqrt{3}$.

5. Hexagonal lattices at low and moderate concentrations

In the main body of the numerical studies we consider the evolution of drops that are initially arranged on a regular hexagonal lattice. The direction of the shear flow coincides with the first, time-independent, base vector of the lattice. In the present section we discuss the motion of initially circular drops at volume fractions less than that corresponding to touching circular drops on a regular hexagonal lattice, $\phi^H_{MAX} = 0.9069$.

The behaviour at small volume fractions is similar to that for the square lattice described in the preceding section. To illustrate the motion at higher volume fractions, in figure 3 we present a series of drop profiles for $Ca = 0.02527$ and volume fraction $\phi = 0.7495$. This particular case was chosen so as to match the geometric configuration of a four-layered suspension in a bounded Couette flow studied by Zhou & Pozrikidis (1993*b*). At this relatively small value of Ca, the drops deform and then evolve in a periodic manner with period $kT = 2/\sqrt{3}$. It is worth noting that the arrangement shown in figure 3(*b, d*) corresponds to a rectangular array of nearly rectangular drops with rounded corners, which identifies the present evolution with that of a rectangular array of non-circular drops. The evolutions of the drop Taylor deformation parameter D and orientation angle θ/π are shown in figure 4(*a*). D varies between 0.04284 to 0.117 while θ oscillates between 0.05274π and 0.231π. These large variations indicate that the drops are subjected to substantial deformations and flipping motions.

Both the qualitative and quantitative features in the evolution of D and θ in figure 4(*a*) are similar to those of the drops in the middle row of the four-layered suspension studied by Zhou & Pozrikidis (1993*b*). The latter are shown in figure 4(*a*) with the plain solid and dashed curves. A comparison suggests that, at this relatively high volume fraction, the presence of boundaries affects the deformation of the drops that are adjacent to the walls, but has little influence on the drops in the layers away from the walls. Furthermore, the general features of the drop deformation are similar to those of three-dimensional drops on a three-dimensional lattice studied by Pozrikidis (1993), and this agreement corroborates the physical relevance of the two-dimensional model.

In figure 4(*b–e*), we present the evolution of the viscometric functions including the effective viscosity μ_{EFF} and normal stress difference $\mathcal{N}$, for $\phi = 0.7495$ and $Ca = 0.02527, 0.2527$. The corresponding results for a four-layered suspension in a channel (Zhou & Pozrikidis 1993*b*) are shown with dashed lines. We observe similar behaviours at long times, but note that the magnitude of oscillations in both μ_{EFF} and $\mathcal{N}$ are larger in the doubly periodic than in the bounded suspensions. This difference is attributed to the fact that the drops adjacent to the walls do not oscillate as strongly as those in the middle layers. As a result, the effective stresses, which are computed in terms of integrals over all the drop interfaces, show oscillations of reduced amplitude in the bounded system.

The differences in the viscometric functions between bounded and unbounded systems become milder as the capillary number is increased from $Ca = 0.02527$ to $Ca = 0.2527$. This is because the relative differences in the deformation of the drops that are adjacent to the walls and those in the bulk of the flow are masked by the enhanced drop deformations due to the weaker action of surface tension. The behaviour of the four-layered suspension is already close to that of the doubly periodic suspension, and the differences are expected to diminish as the number of layers in the bounded system is further increased.

6. Hexagonal lattices at high concentrations

When the volume fraction of the suspended drops is higher than the critical value of $\sqrt{3}\pi/8 \approx 0.6802$, the drops must deform in order to be able to pass each other and engage in periodic motion. This means that there is a lower limit on the capillary number below which surface tension prevents the development of high-curvature regions that is necessary for substantial interfacial deformations. Under

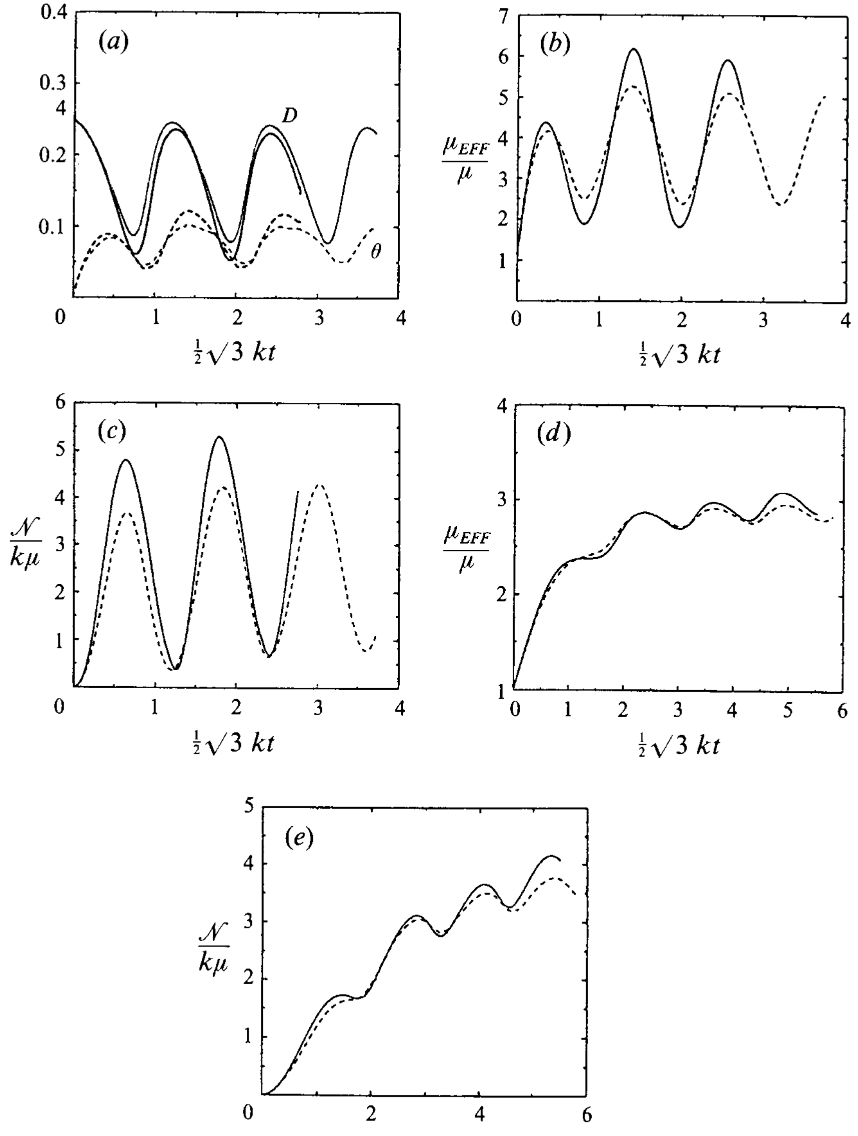

FIGURE 4. Comparison of the geometrical variables and effective stresses of an infinite doubly periodic suspension with those of a four-layer suspension bounded by plane walls studied by Zhou & Pozrikidis (1993*b*). (*a*) Evolution of the Taylor deformation parameter D (solid line) and orientation angle θ (dashed line) of the drops shown in figure 3 for $\phi = 0.7495$ and $Ca = 0.02527$. Bold-faced curves correspond to the present results, plain curves correspond to the results of Zhou & Pozrikidis (1993*b*). (*b*) Evolution of effective viscosity μ_{EFF} for $\phi = 0.7459$ and $Ca = 0.02527$; solid and dashed lines represent, respectively, the results of the present study and those of Zhou & Pozrikidis (1993*b*); (*c*) same as (*b*) but for the normal stress difference $\mathscr{N}$; (*d*) same as (*b*) but with $Ca = 0.2527$; (*e*) same as (*c*) but with $Ca = 0.2527$.

these conditions, the drops will press against each other under the action of the shear flow, and eventually coalesce thus destabilizing the emulsion. On the other hand, there is a maximum value of the capillary number beyond which surface tension is not able to resist the deforming action of viscous stresses, and the drops will continue

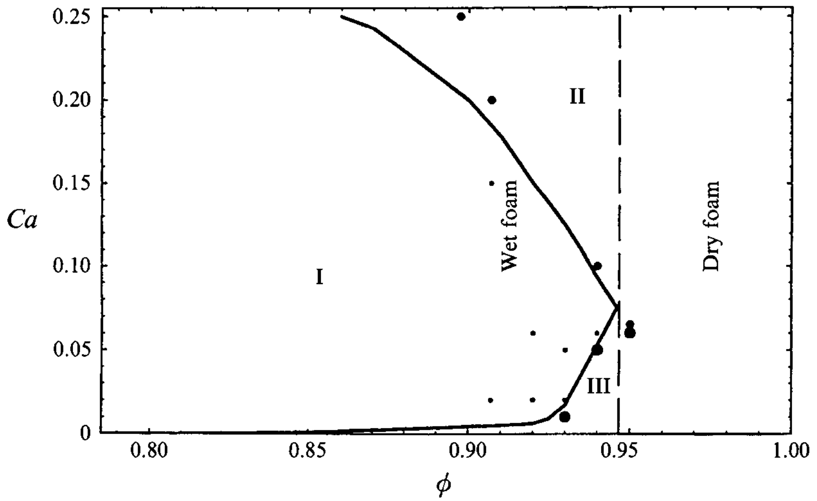

FIGURE 5. Phase diagram for the behaviour of a concentrated emulsion in simple shear flow in terms of (ϕ, Ca). The small dots represent cases where periodic motion is established, the large dots represent cases where the drops coalesce at a finite time, and the medium dots represent cases where the drops exhibit continued elongation. The dashed line separates 'wet' from 'dry' foams.

to elongate due to the straining component of the incident shear flow. Both the upper and lower critical capillary numbers are functions of the volume fraction ϕ.

In figure 5 we present a phase diagram for the behaviour of a concentrated emulsion constructed from the results of the present numerical computations. The volume fraction for circular drops at maximum packing is equal to 0.9069, and higher volume fractions require non-circular initial shapes.

For the combinations of volume fractions and capillary numbers that fall within region I, we observe stable periodic motion. For values within region II, the drops exhibit continued elongation through a sequence of convoluted shapes illustrated in figure 6(*a*–*e*) for $\phi = 0.9069, Ca = 0.2$. Failure to approach a periodic state is evidenced clearly by the monotonic increase in the drop perimeter shown in figure 6(*f*); when the drop shapes become convoluted, the Taylor deformation parameter is a less useful diagnostic. The thickness of the films that separate adjacent drops decreases in time, but a strong tendency for coalescence is not evident in the numerical solution. In region III of figure 5, where Ca is smaller than the lower limit below which surface tension prevents the development of regions with high curvature, the interfaces overlap after a finite time. The details of this motion will be analysed further in §6.5.

Previous theories of foam have classified concentrated emulsions into two categories depending upon the volume fraction (Reinelt & Kraynik 1990). Wet foams occur when the volume fraction falls within the range $0.9069 < \phi < 0.9466$, and their distinguishing feature is that the structure of the periodic cells and associated rheological properties of the suspension vary continuously with the shear strain or unit cell deformation. The lower limit $\phi = 0.9069$ marks the threshold for the onset of thin-film flows that characterize a foam. Below this volume fraction, an analysis in terms of thin films and Plateau borders is not appropriate. Dry foams occur when $\phi > 0.9466$, and their distinguishing feature is that discontinuities in both the structure of the periodic cells and associated rheological properties occur at a certain value of the global strain or deformation. It is interesting to note that region I in

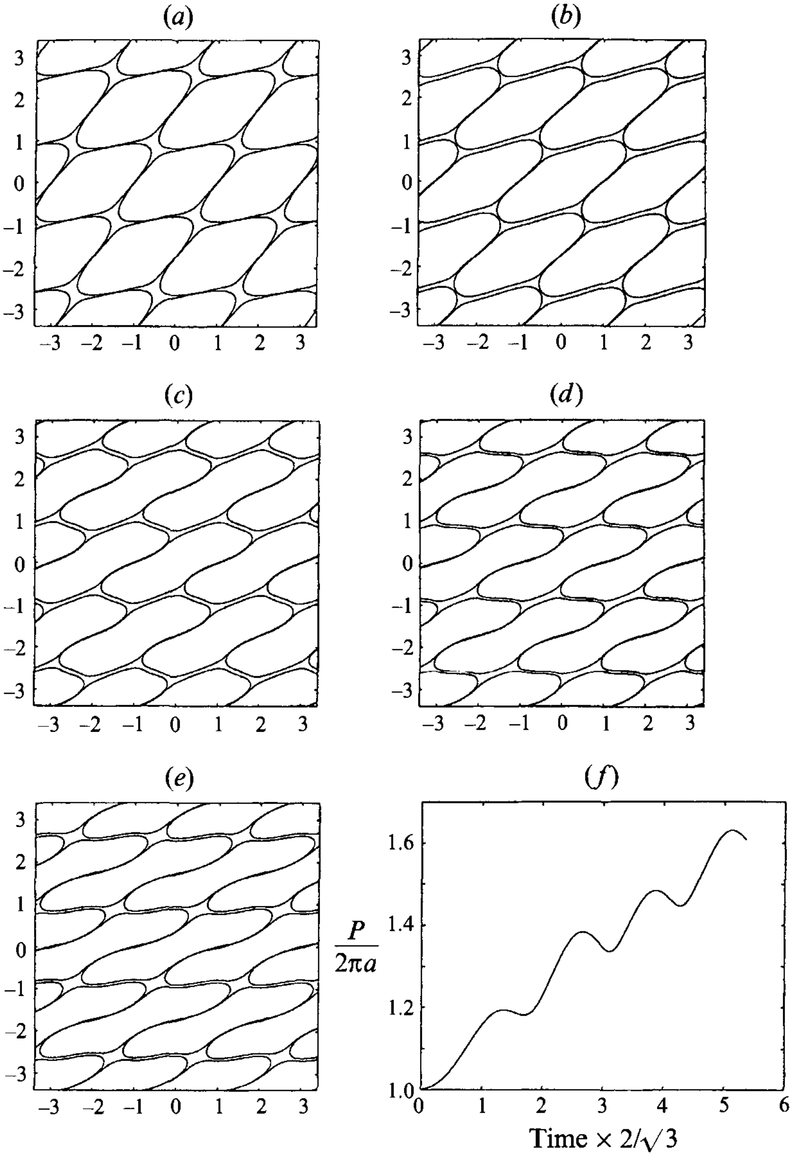

FIGURE 6. A sequence of drop profiles for $\phi = 0.9069$ and $Ca = 0.2$ at times (*a*) $t = T$, (*b*) $2T$, (*c*) $3T$, (*d*) $4T$, (*e*) $5T$, where $kT = 2/\sqrt{3}$; (*f*) the evolution of drop perimeter P.

figure 5 ends near the theoretical threshold $\phi = 0.9466$ which has been established from pure geometrical considerations in previous theories of foam.

6.1. *Geometry of the periodic motion*

Concentrating on region I of figure 5, where periodic motion is established, we analyse the geometry of the evolving cells and discuss the numerical results in comparison with previous theories of foam. At the initial instant, the drops have a regular hexagonal shape with their corners rounded to circular arcs of radius r_0, which are the radii of the Plateau borders. A typical initial arrangement is illustrated in figure 1(*b*). The volume fraction of the dispersed phase ϕ, film thickness $2h_0$, cell size b, and radius of the Plateau borders r_0 are related by

$$r_0 = \frac{\sqrt{3}}{2} b(1-\epsilon) \left(\frac{1-\phi/(1-\epsilon)^2}{1-\pi/(2\sqrt{3})} \right)^{1/2}, \qquad \text{where } \epsilon = \frac{h_0}{\frac{1}{2}\sqrt{3}b}. \tag{6.1}$$

In figure 7 we present a sequence of drop profiles for $\phi = 0.93$, $\epsilon = 0.0244$ and $Ca = 0.02$. Figure 7(*a*) defines the base parallelogram $OABC$ corresponding to a unit cell. The base triangle OAB contains three films $F1, F2$ and $F3$, labelled in the clockwise sense. Inspection of figure 7 shows that, after an initial transient period depicted in figure 7(*a–e*), the suspension evolves in a periodic fashion with period $kT = 2/\sqrt{3}$ which is identical to the period of recurrence of the base lattice (figure 7*e–e′*).

The theory of foam describes the structure of an emulsion in terms of fundamental geometrical modes (Princen 1983). Mode I describes the structure when a Plateau border is connected to its neighbours via three thin films. A transition from Mode I to Mode II occurs when the length of one of the films vanishes. This requires that two Plateau borders coalesce, and the interfaces enclosing the borders join in pairs.

Examining the periodic motion in figure 7 we find a single transition from Mode I (figure 7*e–h*) to Mode II (figure 7*i–k*), then back to Mode I (figure 7*e′*) within each temporal period. Furthermore, we note that the times corresponding to the configurations shown in figure 7(*e′*) and figure 7(*e*) differ by kT, and this suggests that the drops complete one cycle of the so-called 'hopping' motion within each temporal period (Kraynik 1988).

Analysing the evolving geometrical properties of an emulsion is another central theme of the theory of foam, and a point of departure for establishing its effective rheological properties. Princen (1983) developed a quasi-static geometric model to describe the structure of a two-dimensional foam as a function of shear strain. To compare his predictions with the present results, we note that the displacement of the vertices of the unit cell $OABC$ is affine (figure 7*a*), and identify the shear strain with kt.

In figure 8, we present a series of Plateau border configurations at a sequence of characteristic times for $\phi = 0.93$ and $Ca = 0.02$. We observe an initial clockwise rotation of the base triangle OAB connecting three adjacent drop centres, and recession or drainage of film $F2$ into the Plateau borders (figure 8*a–c*). As the motion leads to Mode II, film $F2$ disappears as shown in figure 8(*d*). The Plateau border continues to rotate under the influence of the shear flow, and this leads to a configuration in which the two pairs of films in the unit cell are aligned and the drops assume the shape of parallelograms with rounded corners (figure 8*e*). At that time, a new film is generated at the centre of the Plateau border and the arrangement shown in figure 8(*f*) is rapidly restored. This rapid structural rearrangement causes the drops to overlap at large volume fractions and small capillary number as will be discussed in § 6.5.

The general features of the motion described above are consistent with those postulated in the quasi-static theory of foam (Princen 1983). We note, in particular, that the theory of foam considers the shape shown in figure 8(*e*) to be unstable, which is consistent with the rapid rearrangement observed in the computations. As a minor difference, we observe that the initial configuration with the perfectly hexagonal drops is not fully restored, as is assumed to occur in the theory of foam. Furthermore,

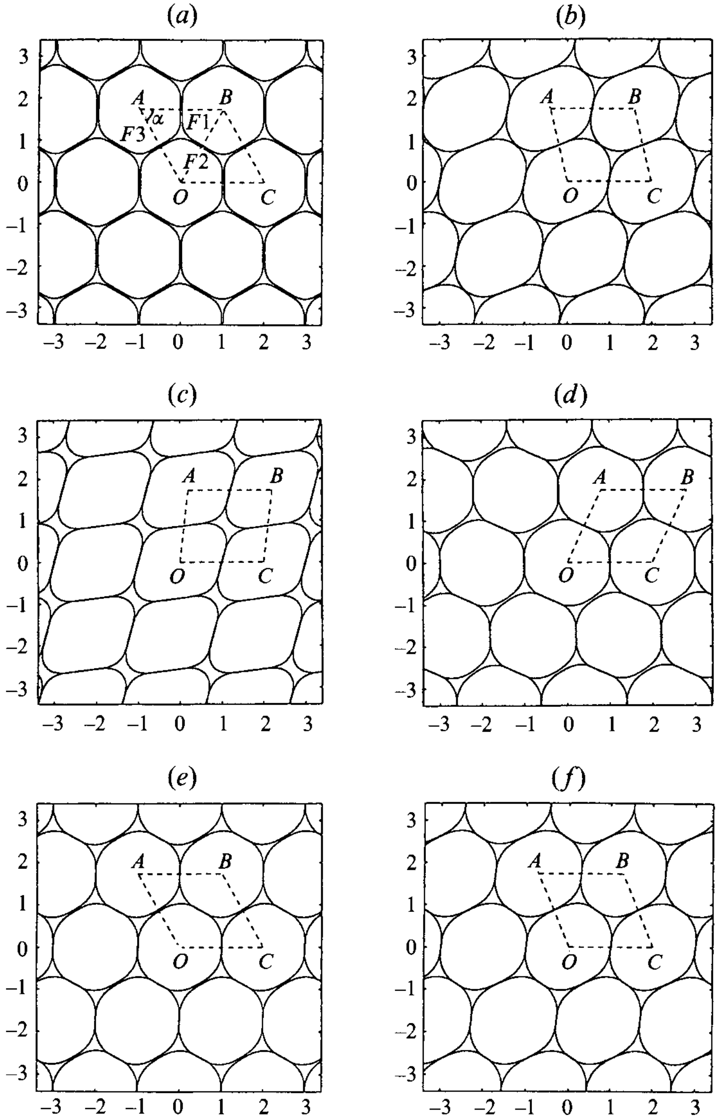

FIGURE 7 (*a–f*). For caption see facing page.

we find that the suspension reaches a periodic state after a finite time period that depends on the initial configuration and Ca for a fixed volume fraction ϕ.

6.2. *Quantitative comparison with the quasi-static theory*

We proceed now to examine the premises and predictions of the quasi-static theory of foam in a more quantitative sense, in the light of the numerical computations. In Princen's (1983) quasi-static analysis, during Mode I the thin films meet at three-fold symmetric triangular Plateau borders whose radius of curvature ρ_0 depends upon the volume fraction ϕ, and the angle subtended by each pair of films is equal to 120°. In figure 9 we plot (*a*) the maximum curvature of each surface enclosing the Plateau border in triangle OAB of figure 7, and (*b*) the angle subtended between each pair of films during Mode I against the angle α defined in figure 7(*a*), for the

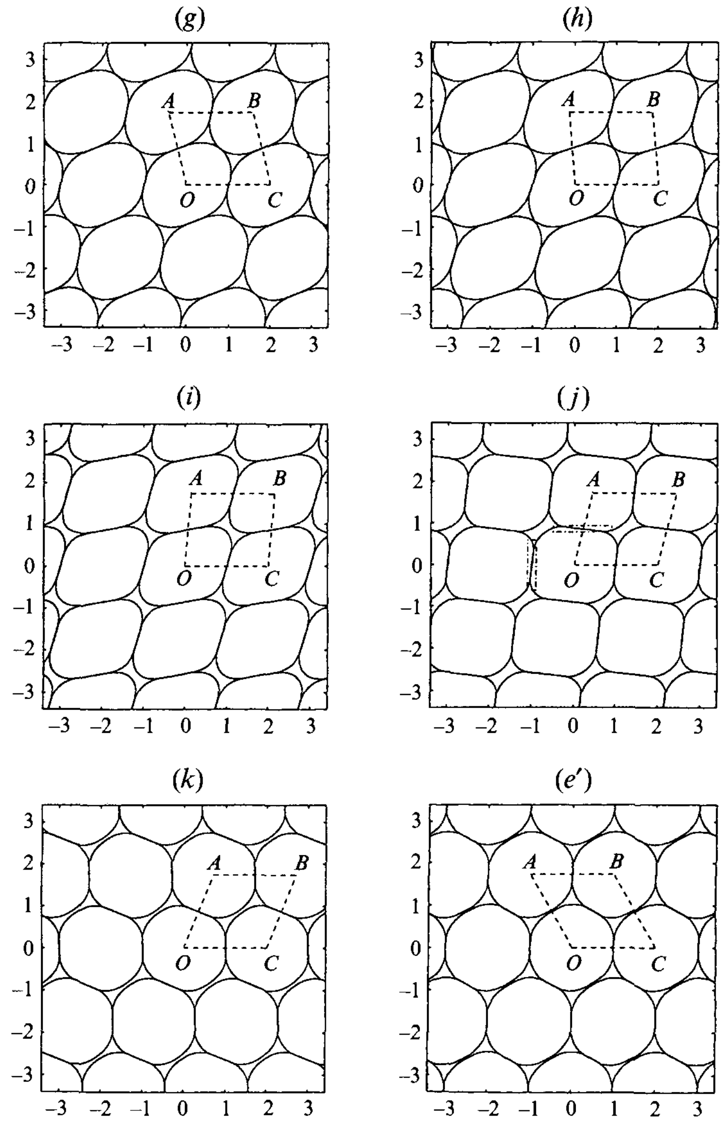

FIGURE 7. A sequence of drop profiles for $\phi = 0.93, \epsilon = 0.0244$ and $Ca = 0.02$ at times (*a*) $t = 0$, (*b*) $0.3T$, (*c*) $0.6T$, (*d*) $0.9T$, (*e*) T, (*f*) $\frac{8}{7}T$, (*g*) $\frac{9}{7}T$, (*h*) $\frac{10}{7}T$, (*i*) $\frac{11}{7}T$, (*j*) $\frac{12}{7}T$, (*k*) $\frac{13}{7}T$, (*e′*) $2T$, where $kT = 2/\sqrt{3}$.

typical case $\phi = 0.93$ and $Ca = 0.02$. Note that α is related to the shear strain within one period of motion by $kt = 1/\sqrt{3} - \cot\alpha$. The numerical results reveal during Mode I that the maximum curvature of the arc connecting $F3$ to $F1$ is substantially lower than that of the other two arcs. Physically, this behaviour may be attributed to the compressive action of the shearing flow in the direction obtained by rotating the x_1-axis 45° clockwise. Correspondingly, the angle subtended by $F1$ and $F2$ is approximately equal to 102°, while the angle between $F3$ and $F1$ is approximately equal to about 138° (figure 9*b*). These results indicate that the assumption of identical radii of curvature for the Plateau border and equal subtended angles between films is not justified under the present of conditions.

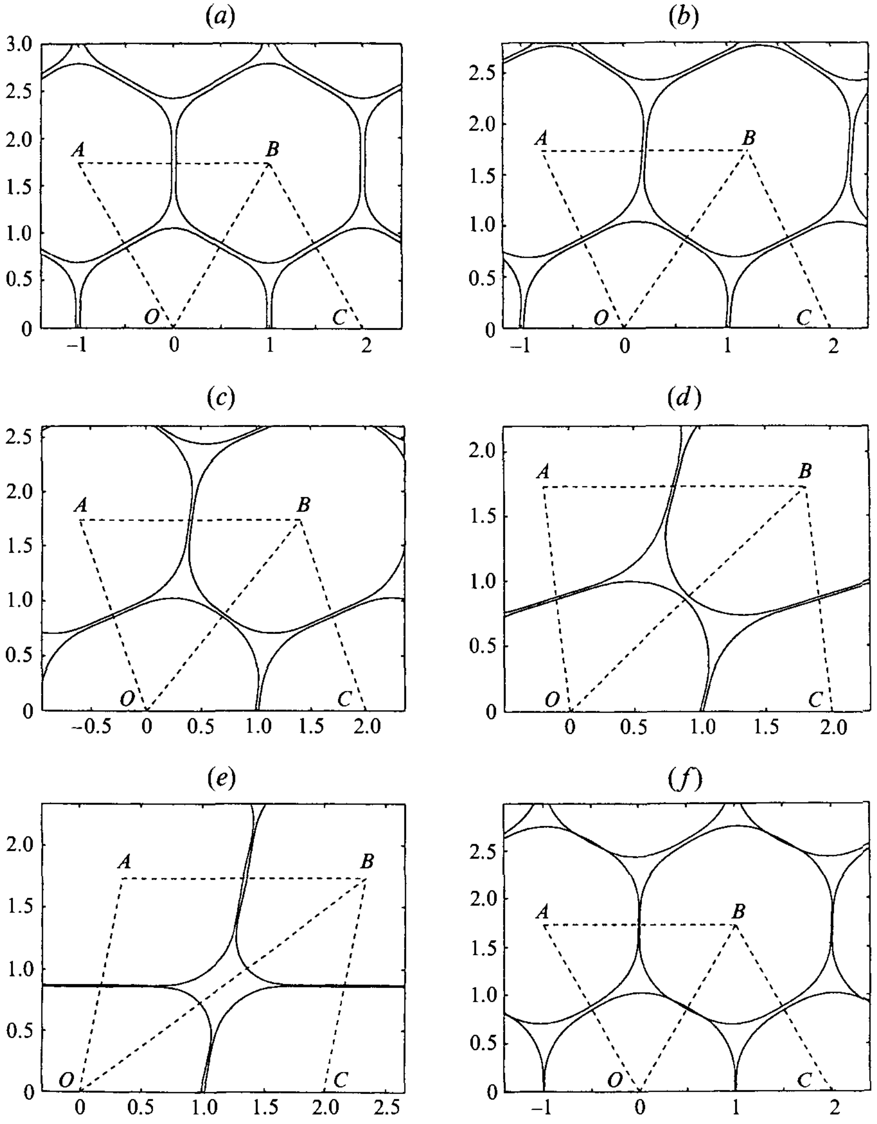

FIGURE 8. A sequence of Plateau border configurations corresponding to figure 7 at times (*a*) $t = 0$, (*b*) $0.1T$, (*c*) $0.2T$, (*d*) $0.4T$, (*e*) $0.67T$, (*f*) T, where $kT = 2/\sqrt{3}$. It should be noted that the drop interfaces do not cross each other when viewed in a magnified frame around the thin film region in panel (*f*).

In figure 9(*c–e*), we plot the extended lengths of the three films as functions of α and compare them to the predictions of the quasi-static theory of foam, shown as solid lines, during Mode I. The extended length of a film is defined as the distance between the centres of the two Plateau borders at which the film ends. Despite the fact that the assumptions of the quasi-static theory are not fully justified, we observe good agreement. For instance, the theory predicts that $F1$ and $F3$ elongate while $F2$ shrinks, and Mode I ends when the two Plateau borders in the unit cell 'contact' each other. Both of these features are observed in the numerical computations.

Furthermore, the quasi-static theory builds on the fact that, when mode II is

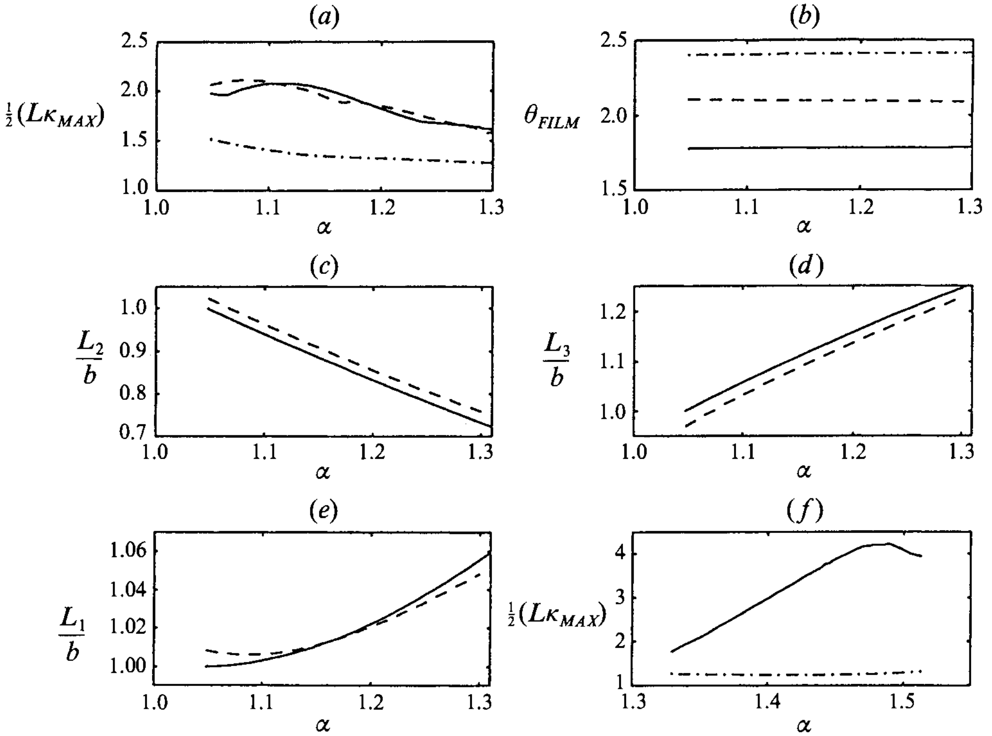

FIGURE 9. Comparison of the numerical results with the predictions of the quasi-static theory of foam. (*a*) Maximum curvature κ_{MAX} of the interfaces enclosing the Plateau border in Mode I plotted against α: -----, interface connecting $F2$ and $F3$; ——, $F1$ and $F2$; —·—, $F3$ and $F1$; (*b*) angles θ_{FILM} subtended between films *vs.* α: -----, angle between $F2$ and $F3$; ——, $F1$ and $F2$; —·—, $F3$ and $F1$; (*c*) extended length of film $F2$, L_2, defined in the text, *vs.* α: ——, predicted by quasi-static theory; -----, obtained from numerical simulation; (*d*) same as (*c*) but for film $F3$; (*e*) same as (*c*) but for film $F1$; (*f*) maximum curvature of the interfaces enclosing the Plateau border in Mode II *vs.* α.

established, the four interfaces of the two merging triangular Plateau borders have identical radii of curvature ρ that are functions of the shear strain. At that point, symmetry requires that the four arcs form two symmetric pairs. In figure 9(*f*) we plot the evolution of the maximum curvature of the two pairs and observe appreciable deviations which underline the limitations of the quasi-static theory. We also find that the computed film lengths, not presented in the figures, show substantial differences from those predicted by the quasi-static analysis. The coalescence of the Plateau borders in Mode II may be interpreted as the result of the compressive action of the applied shear flow, and we find no compelling physical argument that the interfaces must assume identical radii.

6.3. *Flow within the thin films and Plateau borders*

Analysing the flow field within the thin films and Plateau borders allows us to identify the physical mechanisms that govern the evolution of the microstructure.

In figure 10, we illustrate the structure of the velocity field within the thin films $F1, F2, F3$ in figure 7(*a*) and the associated flow at the Plateau border within triangle OAB of figure 7(*a*), in a frame of reference moving with the mid-points of the films or centres of the Plateau borders, for $\phi = 0.93$ and $Ca = 0.02$, at certain characteristic stages of the evolution.

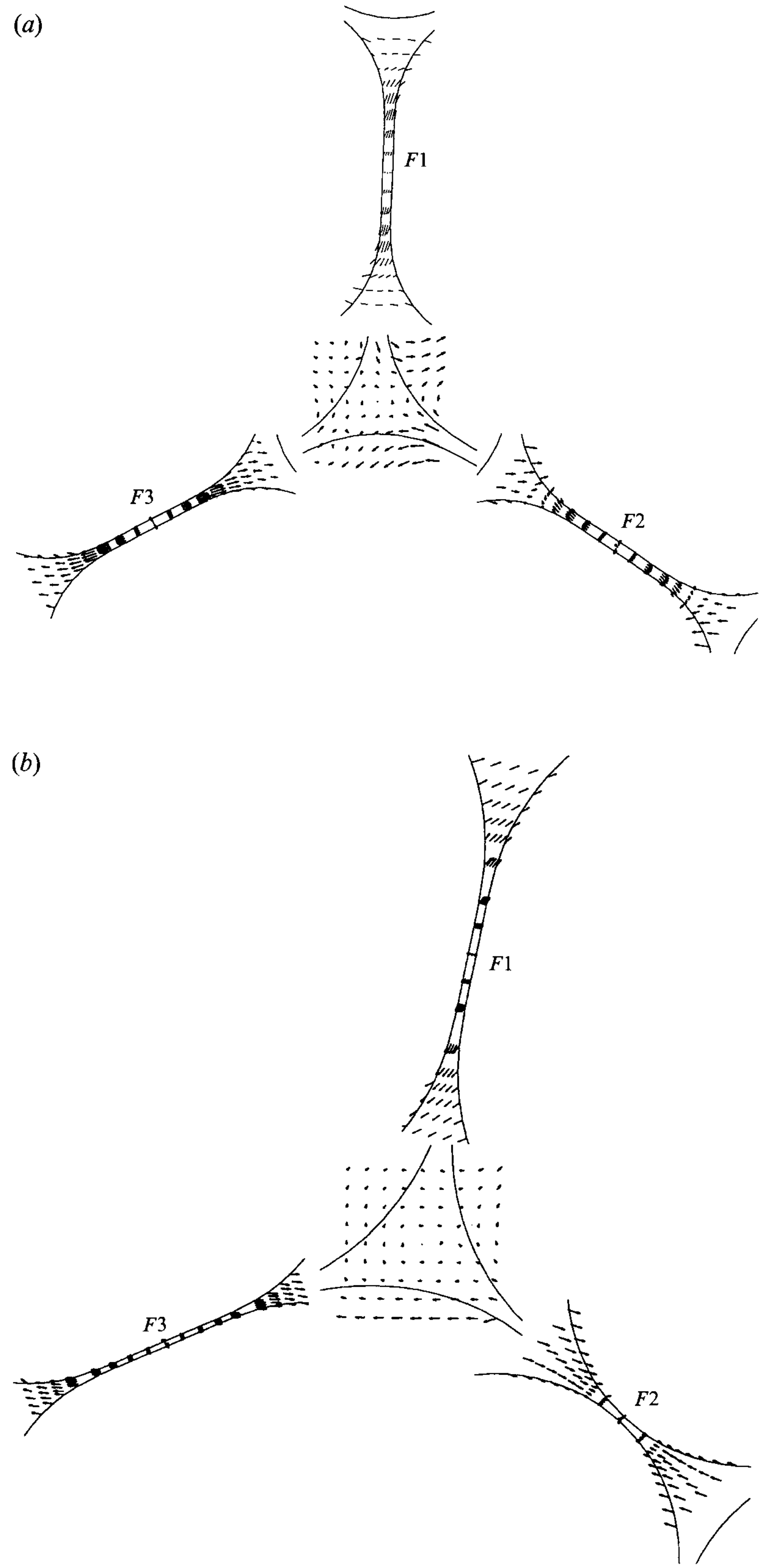

FIGURE 10 (*a*,*b*). For caption see facing page.

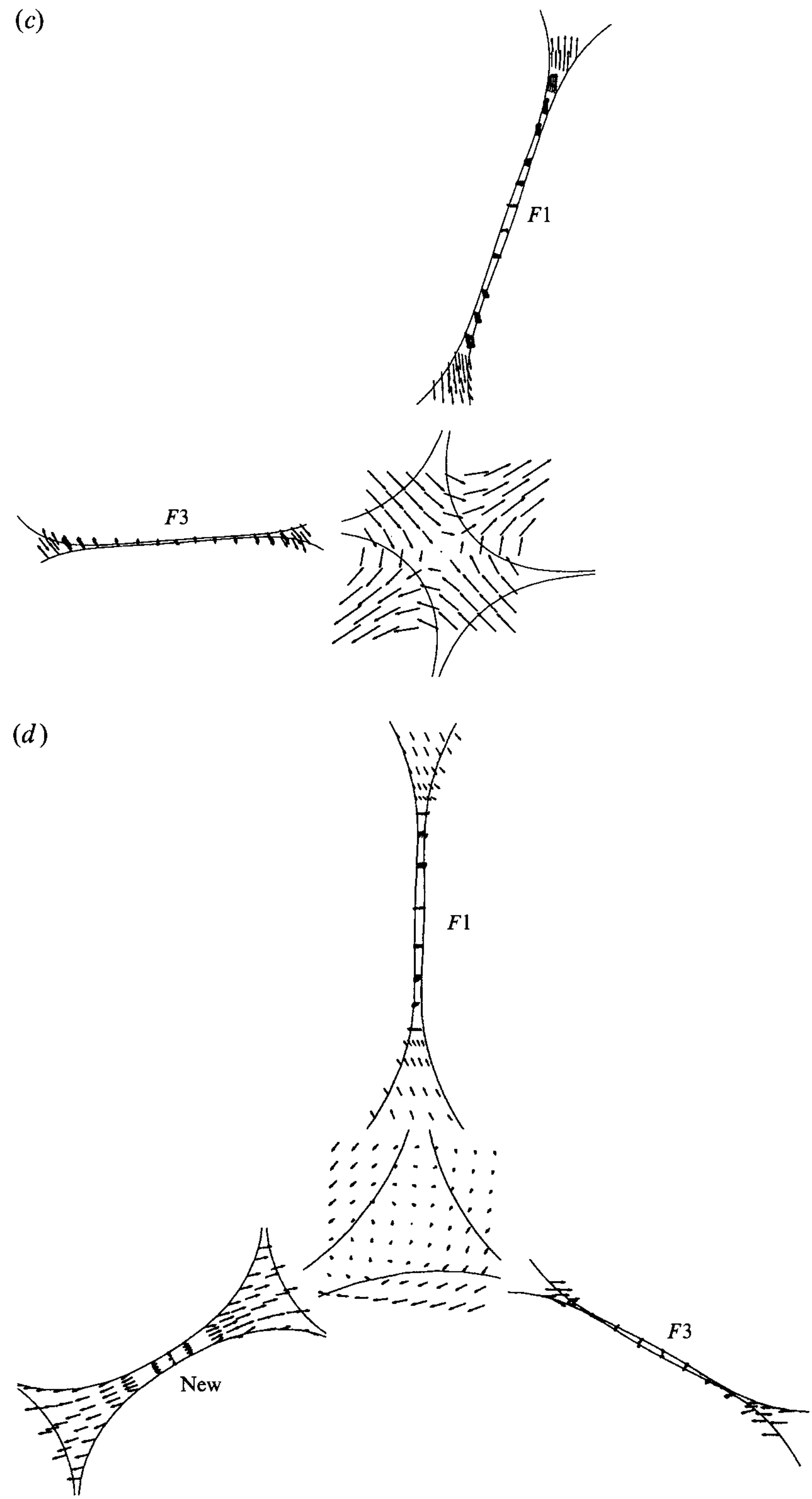

FIGURE 10. The structure of the velocity field within the thin films and Plateau borders at times (*a*) $t = 0.03T$, (*b*) $0.3T$, (*c*) $0.6T$, (*d*) $0.9T$, where $kT = 2/\sqrt{3}$, in a frame of reference moving with the mid-points of the films or centres of the Plateau borders for $\phi = 0.93$ and Ca=0.02. The associated structures of the emulsion at these stages are shown in figure 7.

Figure 10(*a*) corresponds to $t = 0.03T$, a short time after the shear flow has been applied. The associated structure of the emulsion is almost identical to that shown in figure 7(*a*). Figure 10(*a*) shows that the velocity within the films is nearly parallel to the interfaces, the magnitude of the velocity is highest at the transition zones connecting the Plateau borders to the thin films, and the velocity profile in the transition zone is nearly flat with a small parabolic component. Since the pressure at the Plateau borders is lower than that in the thin films, drainage occurs within all three films at this stage. The incident shear flow causes films $F3$ and $F1$ to slowly rotate in the clockwise direction, while it compresses film $F2$, thereby opposing its thinning due to draining. The length of $F2$ decreases as the interfaces peel off the centre of the Plateau borders. The corresponding velocity field at the Plateau border shows that the fluid recedes and causes the expansion of the Plateau borders.

As time proceeds, the thickness of films $F3$ and $F1$ is reduced, but the rotation of the interfaces due to the shear flow has an effect on the rate of drainage, and prevents drop coalescence. We identify this as an important mechanism responsible for the stabilization of the emulsion. The flow within the films at $t = 0.3T$, corresponding to the profiles shown in figure 7(*b*), is illustrated in figure 10(*b*). The shear flow dominates the motion within film $F2$ and causes it to shrink and eventually disappear. The flow field at the Plateau border is characterized by a weak clockwise rotation.

At $t = 0.6T$ the Plateau borders have joined in pairs as shown in figure 10(*c*), $F2$ has virtually disappeared, and the suspension has entered Mode II (figure 7*c*). Film $F3$ has substantially thinned and become aligned with the direction of the shear flow, whereas film $F1$ rotates in the counterclockwise direction against the applied shear flow. The drops tend to roll over each other, reflecting the fact that the flow at the merged Plateau border is characterized by a straining motion with principal axes oriented at 45° with respect to the shear flow. The magnitude of the velocity at the Plateau borders has increased dramatically, indicating that a structural rearrangement is likely to occur at this point. To this end, we digress to remark that the high rate of change of the velocity around the Plateau borders necessitates the use of a high-order adaptive time-advancing scheme, such as the RKF45 method described in §3, to ensure sufficient accuracy.

At the stage corresponding to figure 7(*d*), for $t = 0.9T$, film $F3$ continues to rotate in the clockwise direction, whereas film $F1$ assumes its original vertical orientation with a somewhat reduced length. At that point, the merged Plateau borders separate to form new junctions, and a new film is born. Inspecting figure 10(*d*) shows that the straining motion has relaxed, and the magnitude of the velocity at the newly formed Plateau borders returns to lower levels familiar from the earlier stages.

Previous efforts to model the hydrodynamics of foam have relied on a series of assumptions including the assumption that the interfaces in the transition zone that join the thin films to the Plateau borders are immobilized due to the presence of surfactants (Reinelt & Kraynik 1990). Since our formulation neglects the effects of interfacial rheology, a critical comparison with the predictions of these theories is not appropriate.

6.4. *Effective stresses*

Having described the structure of the foam and velocity field in some detail, we turn to address the behaviour of the viscometric functions including the effective shear viscosity μ_{EFF} and normal stress difference $\mathscr{N}$ defined in (2.7). In figure 11(*a*) we present the evolution of μ_{EFF} and $\mathscr{N}$ for $\phi = 0.93$ and $Ca = 0.02$. At the initial instant, $\mu_{EFF}/\mu = 1$ and $\mathscr{N}/(\mu k) = 0$ because the drops assume a six-fold symmetric shape. Not surprisingly, we find that both μ_{EFF} and $\mathcal{N}$ evolve in a periodic manner after the initial transition period. The amplitude of the oscillations is larger than that observed in § 5 for small and moderate volume fractions. Furthermore, the mean value of the normal stress difference is substantial, which indicates a pronounced elastic behaviour.

Comparing figure 11(*a*) with figure 8 of Reinelt & Kraynik (1990), we find good agreement between the numerical results and the predictions of the quasi-steady theory. Common features are that μ_{EFF} reaches a maximum value right before the middle of each period, and decays rapidly to negative values before it returns to its initial value at the beginning of the next period, and $\mathcal{N}$ is a nearly even function within each temporal period of evolution.

To investigate the effect of Ca on the viscometric functions, in figure 11(*b, c*) we plot μ_{EFF} and $\mathcal{N}$ over one period $kT = 2/\sqrt{3}$ for $\phi = 0.9069$ and $Ca = 0.02, 0.06, 0.08$. To facilitate the comparison, the origin of time has been adjusted so that the curves begin with their mean values. We observe that the amplitude of the oscillations increases as Ca is reduced, and μ_{EFF} assumes negative values when Ca becomes sufficiently small. Furthermore, as Ca is increased, the mean values of both μ_{EFF} and $\mathcal{N}$ decrease, and the foam behaves like a shear-thinning material.

The effect of ϕ on the viscometric functions for a constant capillary number may be deduced from figure 11(*d, e*), illustrating the evolution of μ_{EFF} and $\mathcal{N}$ over one period for $\phi = 0.9069, 0.92, 0.94$ and $Ca = 0.06$. The results show that the average value of μ_{EFF} over one cycle increases monotonically with ϕ, but the average value of $\mathcal{N}$ is rather insensitive to ϕ. Overall, the behaviour of the viscometric functions is similar to that predicted by the quasi-steady theory for wet foams (figure 9 in Reinelt & Kraynik 1990).

To characterize the rheological properties of a suspension in a global sense, we compute the time-average values of the viscometric functions $\overline{\mu}_{EFF}$ and $\overline{\mathcal{N}}$ over one cycle of the periodic motion at large times. Using the film-level lubrication analysis, Reinelt & Kraynik (1990) predicted $\overline{\mu}_{EFF}/\mu \sim Ca^{-1/3}$ and $\overline{\mathcal{N}}/(\gamma/b) \sim C_0 + O(Ca^{2/3})$ for small Ca, where C_0 is a positive constant dependent upon the volume fraction ϕ alone (equations (5.22), (6.1) and (7.2) of Reinelt & Kraynik 1990). In figure 11(*f, g*), we plot $\ln(\overline{\mu}_{EFF}/\mu)$ *vs.* $\ln Ca$ and $\overline{\mathcal{N}}/(\gamma/b)$ *vs.* Ca for $\phi = 0.9069$ and $Ca = 0.05, 0.06, 0.08, 0.1$. Assuming a power-law relation of the form $\overline{\mu}_{EFF}/\mu \sim Ca^{\beta}$, we find that the exponent β increases from -0.8 to -0.386 as Ca is decreased. The numerical results in figure 11(*f*) suggest that as Ca becomes smaller, the exponent in the assumed power-law relation approaches the asymptotic value predicted by the quasi-steady theory. Furthermore, as shown in figure 11(*g*), $\overline{\mathcal{N}}/(\gamma/b)$ oscillates about the value 0.0655, which is very close to the value read from figure 14 of Reinelt & Kraynik (1990). Overall, although there are differences in the assumed physical conditions, we observe satisfactory agreement with the predictions of the quasi-steady analysis.

6.5. *Coalescence of drops and collapse of thin films*

The numerical results indicated that, at sufficiently large values of ϕ and small values of Ca, the interfaces cross each other and the drops coalesce in a finite time. A typical configuration with overlapped interfaces is illustrated in figure 12 for $\phi = 0.94$ and $Ca = 0.05$. This behaviour appears to be physical, as corroborated by the fact that refining the spatial resolution or decreasing the size of the time step does not prevent coalescence.

To provide a physical explanation and establish criteria for coalescence, we recall that the drops tend to press against each other, but also roll over each other under the

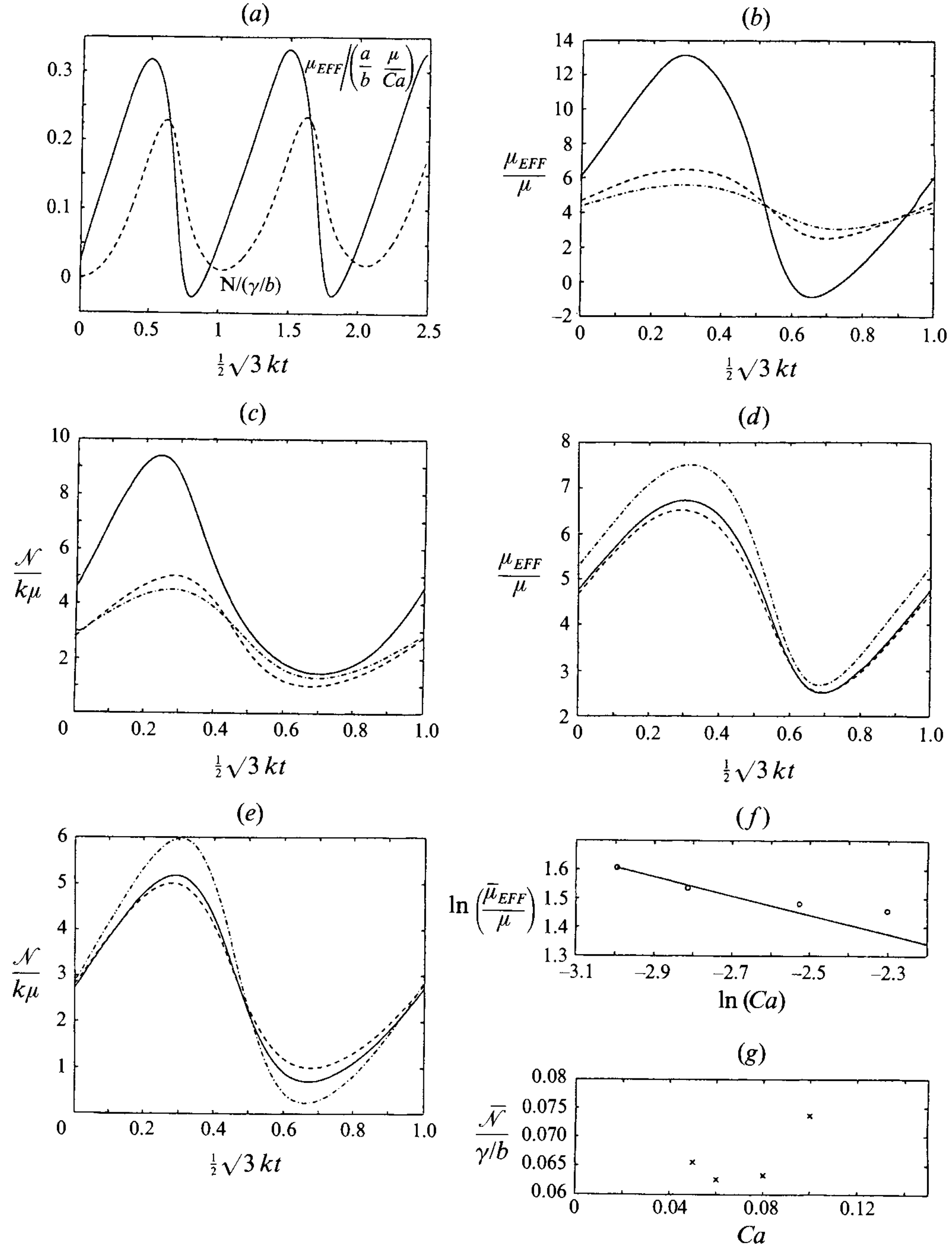

FIGURE 11. (a) Evolution of effective viscosity μ_{EFF}(——) and the normal stress difference $\mathscr{N}$(-----) for $\phi = 0.93, Ca = 0.02$; (b) effective viscosity μ_{EFF} for $\phi = 0.9069$ for different capillary numbers Ca: ——, 0.02; -----, 0.06; —·—, 0.08; (c) same as (b) but for the normal stress difference $\mathscr{N}$; (d) effective viscosity μ_{EFF} for $Ca = 0.06$ at different volume fractions ϕ:-----, 0.9069; ——, 0.92; —·—, 0.94; (e) same as (d) but for normal stress difference $\mathscr{N}$; (f) $\ln(\bar{\mu}_{EFF}/\mu)$ vs. $\ln Ca$ for $\phi = 0.9069$ and $Ca = 0.05, 0.06, 0.08, 0.1$; the solid line shows the power-law relation for $\bar{\mu}_{EFF}$ predicted by Reinelt & Kraynik (1990); (g) $\bar{\mathscr{N}}/(\gamma/b)$ vs. Ca for $\phi = 0.9069$ and $Ca = 0.05, 0.06, 0.08, 0.1$.

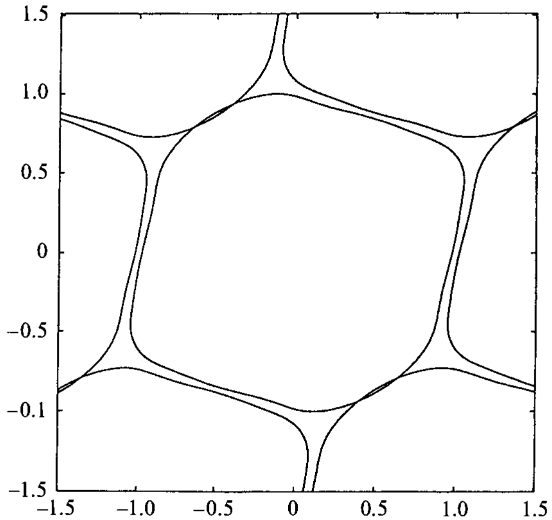

FIGURE 12. Overlapping drops in a dry foam for $\phi = 0.94$ and $Ca = 0.05$ at time $t = 0.97T$.

influence of the incident shear flow. Previous asymptotic analyses of the flow in the lubrication zone between two colliding drops indicate that the interfaces will coalesce in a finite time (Davis, Schonberg & Rallison 1989), and this suggests that coalescence will occur if a particular section of an interface is allowed to press against another section for a sufficiently long time. In the present problem, the time of contact is determined by the rolling motion which, in turn, depends upon the capillary number and volume fraction. When periodic motion is established, the rolling motion is fast enough so that the films are restructured before the interfaces have had enough time to coalesce.

It is possible to continue the computations after coalescence by assuming that the thin films do not rupture but merge to form a black film of vanishing thickness. Implementing this extension is under current investigation.

The authors wish to thank Professor Russell Caflisch for helpful discussions. This research is supported by the National Science Foundation Grant under grant CTS-9216176 and the Department of Energy. Partial support was provided by the Exxon Education Foundation. Computer time is provided by the San Diego Supercomputer Center.

Appendix. Computation of the two-dimensional doubly periodic Green's function

We consider the flow due to a doubly periodic lattice of two-dimensional point forces in the (x, y)-plane. One of the point forces is located at the position $\boldsymbol{x}_0$ and the rest of them are separated by the lattice vectors

$$\boldsymbol{X}_l = i_1 \boldsymbol{a}_1 + i_2 \boldsymbol{a}_2 \tag{A 1}$$

where $\boldsymbol{a}_1, \boldsymbol{a}_2$ are two arbitrary base vectors in the (x, y)-plane and i_1, i_2 are two integers.

As a preliminary, we introduce the reciprocal base vectors $\boldsymbol{b}_1$ and $\boldsymbol{b}_2$ defined as

$$\boldsymbol{b}_1 = \frac{2\pi}{A} \boldsymbol{a}_2 \times \boldsymbol{k}, \quad \boldsymbol{b}_2 = \frac{2\pi}{A} \boldsymbol{k} \times \boldsymbol{a}_1, \tag{A 2}$$

where $A = |\boldsymbol{a}_1 \times \boldsymbol{a}_2|$ is the area of one periodic cell and $\boldsymbol{k}$ is the unit vector along the z-axis. Based on (A 2), we construct the reciprocal lattice in wavenumber space with lattice points at

$$\boldsymbol{\alpha}_\lambda = j_1 \boldsymbol{b}_1 + j_2 \boldsymbol{b}_2 \tag{A 3}$$

where j_1, j_2 are two integers. The physical and reciprocal lattice points satisfy the equation

$$\boldsymbol{X}_l \cdot \boldsymbol{\alpha}_\lambda = 2\pi m \tag{A 4}$$

where m is an integer.

The velocity field due to the above doubly periodic array may be expressed in terms of the corresponding Green's function $\mathbf{G}^{DP}$ as $u_i = 1/(4\pi\mu) G_{ij}^{DP} g_j$, where $\boldsymbol{g}$ is the strength of each of the point forces (Pozrikidis 1992, Chapter 3). Expanding the velocity and pressure in Fourier series, and substituting them into the Stokes equation and continuity equation, provides us with

$$G_{ij}(\boldsymbol{x}, \boldsymbol{x}_0) = \sum_{\lambda=0}^{\infty} \exp[-\mathrm{i}\boldsymbol{\alpha}_\lambda \cdot (\boldsymbol{x} - \boldsymbol{x}_0)] \frac{1}{|\boldsymbol{\alpha}_\lambda|^2} \left(\delta_{ij} - \frac{\alpha_{\lambda_i} \alpha_{\lambda_j}}{|\boldsymbol{\alpha}_\lambda|^2} \right). \tag{A 5}$$

Unfortunately, the sum in (A 5) is slowly convergent, and this makes the computation of the Green's function in terms of Fourier sums prohibitively expensive. To overcome this difficulty in the analogous case of a three-dimensional flow due to a three-dimensional array of point forces, Brady *et al.* (1988) and Pozrikidis (1993) recast the Fourier series in terms of two Ewald sums developed earlier by Beenaker (1986). The procedure is outlined in the appendix of Pozrikidis (1993). The final expression contains a lattice sum in real space, and a complementary lattice sum in reciprocal space. An analogous development is possible for the present case of two-dimensional flow, but the final expression involves integrals of Bessel functions over infinite domains that are costly to compute.

A better way of computing the two-dimensional Green's function is to integrate its three-dimensional counterpart in the z-direction over one period (Li & Pozrikidis 1995). The final result is

$$\mathbf{G}^{DP}(\boldsymbol{x}, \boldsymbol{x}_0) = \sum_{k=0}^{\infty} \mathbf{G}^{(1)}(\boldsymbol{x} - \boldsymbol{x}_0 - \boldsymbol{X}_l) + \frac{4\pi}{A} \sum_{\lambda=0, |\boldsymbol{\alpha}_\lambda| \neq 0}^{\infty} \mathbf{G}^{(2)}(\boldsymbol{x} - \boldsymbol{x}_0, \boldsymbol{\alpha}_\lambda), \tag{A 6}$$

where

$$G_{ij}^{(1)}(\boldsymbol{X}) = \delta_{ij} \int_0^\infty \frac{C(\xi(|\boldsymbol{X}|^2 + z^2)^{1/2})}{(|\boldsymbol{X}|^2 + z^2)^{1/2}} \,\mathrm{d}z + x_i x_j \int_0^\infty \frac{D(\xi(|\boldsymbol{X}|^2 + z^2)^{1/2})}{(|\boldsymbol{X}|^2 + z^2)^{3/2}} \,\mathrm{d}z \tag{A 7}$$

and

$$G_{ij}^{(2)}(\boldsymbol{X}, \boldsymbol{\alpha}) = \cos(\boldsymbol{\alpha} \cdot \boldsymbol{X}) \frac{1}{|\boldsymbol{\alpha}|^2} \left(\delta_{ij} - \frac{\alpha_i \alpha_j}{|\boldsymbol{\alpha}|^2} \right) (1 + \tfrac{1}{4}\omega^2 + \tfrac{1}{8}\omega^4) \exp(-\tfrac{1}{4}\omega^2) \tag{A 8}$$

with $\omega = |\boldsymbol{\alpha}|/\xi$. The functions C and D are given by

$$C(x) = \operatorname{erfc}(x) + \frac{2}{\pi^{1/2}}(2x^2 - 3)x \exp(-x^2), \tag{A 9}$$

and

$$D(x) = \operatorname{erfc}(x) + \frac{2}{\pi^{1/2}}(1 - 2x^2)x \exp(-x^2). \tag{A 10}$$

The terms within both sums in (A 6) decay at an exponential rate with respect to their arguments.

The variable ξ is a free parameter of the Ewald decomposition method that determines the relative contributions of the sums in real and reciprocal space. As ξ tends to infinity, the contribution of the sum in physical space is reduced, and we recover the Fourier solution (A 5). As ξ tends to zero, the contribution of the sum in reciprocal space is reduced, and we obtain the Green's function as a sum of the two-dimensional Stokeslets associated with the individual point forces. When $\xi = 0$, however, the sum diverges, indicating that the limit is singular.

The exponential decay of the terms within the sums in (A 6) allows us to truncate the limits of summation to a finite level that depends on the value of ξ. Given the shape and size of a unit cell, there is an optimal value of ξ that minimizes the computational effort for a specified level of accuracy. Since the summation in real space, expressed by the first term in (A 6), involves the numerical evaluation of two integrals, whose computation will be discussed later in this appendix, we choose a value of ξ that is large enough so that the computation is biased towards the reciprocal lattice. For example, when $\boldsymbol{a}_1 = (2, 0)$ and $\boldsymbol{a}_2 = (-1, \sqrt{3})$, we choose $\xi = 2.3$ which sums over 9 lattice points in real space and 64 lattice points in reciprocal space, yielding accuracy up to the seventh significant figure. Each evaluation of the Green's function requires $O(10^{-4})$ seconds on the CRAY C90 of the San Diego Supercomputer Center.

Both integrands in (A 7) become singular as the variable of integration z and $|\boldsymbol{X}|$ tend to zero. To compute the first integral in this limit, we rewrite it in the form

$$I(\xi, r) = \int_0^\infty \frac{C(\xi(r^2 + z^2)^{1/2})}{(r^2 + z^2)^{1/2}}\, \mathrm{d}z. \tag{A 11}$$

We note that the function $C(x)$ decays like $\exp(-x^2)$ for large values of x, truncate the domain of integration to a finite interval $[0, N(\xi)]$, where $N(\xi)$ is a positive constant dependent on the value of ξ, and subtract off the singularity by writing

$$\begin{aligned} I(\xi, r) &\approx \int_0^{N(\xi)} \frac{C(\xi(r^2 + z^2)^{1/2})}{(r^2 + z^2)^{1/2}}\, \mathrm{d}z \\ &= \int_0^{N(\xi)} \frac{C(\xi(r^2 + z^2)^{1/2}) - C(0)}{(r^2 + z^2)^{1/2}}\, \mathrm{d}z + C(0) \int_0^{N(\xi)} \frac{1}{(r^2 + z^2)^{1/2}}\, \mathrm{d}z \\ &= \int_0^{N(\xi)} \frac{C(\xi(r^2 + z^2)^{1/2}) - 1}{(r^2 + z^2)^{1/2}}\, \mathrm{d}z + \ln((r^2 + N^2(\xi))^{1/2} + N(\xi)) - \ln(r). \end{aligned} \tag{A 12}$$

The regular integral on the right-hand side of (A 12) is computed using the 20-point Gauss–Legendre quadrature. A similar method is applied for the computation of the second integral in (A 7).

REFERENCES

BATCHELOR, G. K. 1970 The stress system in a suspension of force-free particles. *J. Fluid Mech.* **41**, 545–570.

BEENAKER, C. W. J. 1986 Ewald sum of the Rotne-Prager tensor. *J. Chem. Phys.* **85**, 1581–1582.

BRADY, J. F., PHILLIPS, R. J., LESTER, J. C. & BOSIS, G. 1988 Dynamic simulation of hydrodynamically interacting suspensions. *J. Fluid Mech.* **195**, 257–280.

DAVIS, R. H., SCHONBERG, J. A. & RALLISON, J. M. 1989 The lubrication force between two viscous drops. *Phys. Fluids* A **1**, 77–81.

KENNEDY, M. R., POZRIKIDIS, C. & SKALAK, R. 1994 Motion and deformation of liquid drops and the rheology of dilute emulsions in simple shear flow. *Computers and Fluids* **23**, 251–278.

Khan, S. A. 1985 Rheology of large gas fraction liquid foams. PhD thesis, MIT, Cambridge.

Khan, S. A. & Armstrong, R. C. 1986 Rheology of foams: I. Theory for dry foams. *J. Non-Newtonian Fluid Mech.* **22**, 1–22.

Khan, S. A. & Armstrong, R. C. 1987 Rheology of foams: II. Effects of polydispersity and liquid viscosity for foams having gas fraction approaching unity. *J. Non-Newtonian Fluid Mech.* **25**, 61–92.

Kraynik, A. M. 1988 Foam flow. *Ann. Rev. Fluid Mech.* **20**, 325–357.

Kraynik, A. M. & Hansen, M. G. 1986 Foam and emulsion rheology: a quasistatic model for large deformations of spatially periodic cells. *J. Rheol.* **30**, 409–439.

Kraynik, A. M. & Hansen, M. G. 1987 Foam rheology: a model of viscous phenomena. *J. Rheol.* **31**, 175–205.

Li, X. & Pozrikidis, C. 1995 On the computation of periodic Green's functions of Stokes flow with application to flow through two-dimensional random porous media. *J. Engng Maths* (submitted).

Mysels, K. J., Shinoda, K. & Frankel, S. 1959 *Soap Films: Studies of Their Thinning*. Pergamon.

Pacetti, S. D. 1985 Structural modeling of foam rheology. MS thesis, University of Texas, Houston.

Pozrikidis, C. 1992 *Boundary Integral and Singularity Methods for Linearized Viscous Flow*. Cambridge University Press.

Pozrikidis, C. 1993 On the transient motion of ordered suspensions of liquid drops. *J. Fluid Mech.* **246**, 301–320.

Pozrikidis, C. 1994 Effects of surface viscosity on the finite deformation of a liquid drop and the rheology of dilute emulsions in simple shearing flow. *J. Non-Newtonian Fluid Mech.* **51**, 161–178.

Princen, H. M. 1979 Highly concentrated emulsions: I. Cylindrical systems. *J. Colloid Interface Sci.* **71**, 55–66.

Princen, H. M. 1983 Rheology of foams and highly concentrated emulsions: I. Elastic properties and yield stress of a cylindrical model system. *J. Colloid Interface Sci.* **91**, 60–75.

Reinelt, D. A. & Kraynik, A. M. 1989 Viscous effects in the rheology of foams and concentrated emulsions. *J. Colloid Interface Sci.* **132**, 491–503.

Reinelt, D. A. & Kraynik, A. M. 1990 On the shearing flow of foams and concentrated emulsions. *J. Fluid Mech.* **215**, 431–455.

Schwartz, L. W. & Princen, H. M. 1987 A theory of extensional viscosity for flowing foams and concentrated emulsions. *J. Colloid Interface Sci.* **118**, 201–211.

Stone, H. 1994 Dynamics of drop deformation and breakup in viscous fluids. *Ann. Rev. Fluid Mech.* **26**, 65–102.

Zhou, H. & Pozrikidis, C. 1993*a* The flow of suspensions in channels: single files of drops. *Phys. Fluids* A **5**, 311–324.

Zhou, H. & Pozrikidis, C. 1993*b* The flow of ordered and random suspensions of two-dimensional drops in a channel. *J. Fluid Mech.* **255**, 103–127.